

RAPID COMMUNICATION

Enhanced photoresponse of ZnO nanorods-based self-powered photodetector by piezotronic interface engineering



Zheng Zhang^{a,1}, Qingliang Liao^{a,1}, Yanhao Yu^b, Xudong Wang^{b,*},
Yue Zhang^{a,c,**}

^aState Key Laboratory for Advanced Metals and Materials, School of Materials Science and Engineering, University of Science and Technology Beijing, China

^bDepartment of Materials Science and Engineering, University of Wisconsin-Madison, WI 53706, United States

^cKey Laboratory of New Energy Materials and Technologies, University of Science and Technology Beijing, Beijing 100083, China

Received 3 July 2014; accepted 22 July 2014
Available online 6 August 2014

KEYWORDS

Self-powered photo-detector;
Interface engineering;
Piezotronic effect;
Metal-insulator-semiconductor;
ZnO

Abstract

Strain-induced piezopolarization can effectively engineer the interfacial electronic properties of a piezo-semiconductor junction, and thereby improve the performance of corresponding electronic devices. In this work, a metal-insulator-semiconductor (Pt/Al₂O₃/ZnO) based self-powered (SP) photodetector has been developed. The photodetector has sensitive response to the light illumination without any external bias. Applying an ultrathin dielectric layer and piezotronic effect are used as two effective strategies for interface engineering to enhance the photoresponse properties. The dielectric layer can significantly enhance the effective Schottky barrier height (SBH). In addition, the SBH can be actively modulated by the piezopolarization induced built-in electric field variation under compressive strains. Thus, the photoresponse properties of the SP photodetector are largely improved by the SBH enhancement. The responsivity and detectivity of the SP photodetector are increased by 2.77 times and 2.78 times, respectively under a compressive strain of -1.0% . According to the Schottky junction

*Corresponding author.

**Corresponding author at: State Key Laboratory for Advanced Metals and Materials, School of Materials Science and Engineering, University of Science and Technology Beijing, China

E-mail addresses: xudong@engr.wisc.edu (X. Wang), yuezhong@ustb.edu.cn (Y. Zhang).

¹These authors contribute equally.

principle, it can be concluded that the piezotronic effect occurs strongly at the interface and gradually decays towards the quasi-neutral region of the junction.

© 2014 Elsevier Ltd. All rights reserved.

Introduction

Nanotechnology has been considered as a valid approach to solve the growing threat of global energy crises. Aiming toward highly intelligent and efficient integration, low power consumption, extremely sensitive and rapid response, and environmental benignity, a variety of novel nanodevices has been demonstrated, including solar cells [1], nanogenerators [2-4], light-emitted-diodes (LEDs) [5], sensors [6], and electronics [7]. For junction based semiconductor devices, interface engineering is an effective way to improve the performance by optimizing the crystal lattice structures, electronic band structure, barrier height, space charge region, and surface states [8]. Recently it has become a promising method to modify the interfacial physical and chemical properties at the junction area utilizing the piezotronic effect which is the coupling of semiconductor properties and piezoelectric effects [9]. For a strained piezoelectric semiconductor, such as ZnO, an ionic-displacement takes place inside ZnO inducing piezoelectric polarization that can modulate the carrier concentration, barrier height and built-in electric field at the interface [10,11]. The piezotronic effect has been used to monitor the performances of heterojunction solar cells, photoelectrochemical anodes, and LEDs [12-15].

On the other hand, piezoelectric nanogenerator is a direct application of piezoelectric effect in ambient mechanical energy harvesting, which leads to a mass of self-powered (SP) nanodevices and nano-systems [16,17]. A series of SP nanodevices composed of nanogenerators and sensing units have been developed to detect vibration [18], magnetism [19], and photons [20]. The most effective SP device is to integrate the powering and sensing functions in the same building block. Based on this concept, a new type of fast and sensitive SP photodetector was demonstrated using the built-in electric field at the junction area of a pn junction [21,22] or a metal-semiconductor (MS) contact [23,24] to separate the photogenerated electron-hole pairs (EHPs) under illumination without a bias [23,25]. For an MS photodetector, the deep depletion region formed in the semiconductor provides strong built-in electric-field to separate EHPs [26,27]. Furthermore, a thin insulator layer can be employed between semiconductor and metal electrode forming a metal-insulator-semiconductor (MIS) contact, where the insulator layer reduces the tunneling current from metal to semiconductor and improves the reliability and performance. The performance of a ZnO based SP photodetector might be effectively improved by the strain-induced piezopolarization at the ZnO-Pt interface.

In this work, an MIS based SP photodetector was developed, where the insulator layer was an Al₂O₃ thin film prepared by atom layer deposition (ALD). The photoresponses of the SP photodetector were enhanced by the modulation of barrier heights and built-in electric field as a

result of piezo-induced negative polarization, which was further evidenced by the investigation of the resistance variation at junction area under compressive strains.

Experimental sections

Growth of ZnO Nanorod arrays (NRAs)

The ZnO NRAs were grown on FTO substrates using hydrothermal method. The colloid seed solution was prepared by dissolving zinc acetate [Zn(CH₃COO)₂·2H₂O] in ethanol with a concentration of 0.05 M. Several drops of colloid seed solution were applied onto a cleaned FTO substrate to cover the entire substrate surface. The substrate was dried at room temperature and then annealed at 350 °C in air for 30 min. The precursor solution was prepared by dissolving Zinc nitrate hexahydrate [Zn(NO₃)₂·6H₂O] and hexamethylenetetramine (HMTA) [(CH₂)₆N₄] in deionized water with an equal concentration of 0.1 M. The substrate coated with ZnO seed layer was immersed in the precursor solution at 95 °C for 6 h without stirring.

Deposition of Al₂O₃ layer by atomic layer deposition (ALD)

A home-made ALD system was applied to carry out the thin film coating of Al₂O₃ on ZnO NR surface. The amount of trimethylaluminum and H₂O vapor supply were controlled by two solenoid valves. The target substrate was loaded in a quartz tube and placed at the position 5 cm away from the precursor inlet nozzle. N₂ gas with 40 sccm flow rate was introduced into the chamber to serve as the carrier gas and provide 3.3 Torr system base pressure. During the coating process, the system temperature was kept at 100 °C. Trimethylaluminum and H₂O was pulsed into the reaction chamber separately with a pulsing time of 500 ms and followed by 60 s N₂ purging. Therefore, one deposition cycles involves 500 ms of H₂O pulse+60 s of N₂ purging+500 ms of trimethylaluminum pulse+60 s of N₂ purging. After 20 cycles of deposition, the chamber was allowed to cool down naturally under N₂ flow.

Device fabrication

The Pt electrode was prepared by depositing a thin film of Ti/Pt onto a highly conductive Si substrate. The Si substrate with a resistivity of 0.001-0.005 Ω/cm was sliced into 1.5 mm × 1.5 mm square pieces. The Si substrate was cleaned by Piranha solution (H₂SO₄:H₂O₂=60: 1, 100 °C), SC-1 (NH₄OH: H₂O₂: DI=1: 1: 5, 75 °C), SC-2 (HCl: H₂O₂: DI=1: 1: 5, 75 °C), and diluted HF (HF: DI=1: 50) solution. The substrate was then loaded into CHA metal evaporator for oxide free surface. The Ti/Pt (20/130 nm) film was deposited by e-beam evaporation under the base pressure of less than 2.1 × 10⁻⁶ Torr. The evaporation rate

was controlled in 0.5 A/s to acquire a uniform coating. The thickness of each metal was monitored by a thickness monitor crystal. Figure S2 in SI shows the image morphology and the electrical property of the Pt electrode. A piece of Pt electrode was placed on the top surface of the Al₂O₃-covered ZnO NRAs. The Pt electrode and bottom FTO substrate were connected to the external circuit with silver paste and packaged with epoxy, as shown in Figure 1a. A 150 W Xe arc lamp serves as the light source illuminating the FTO electrode of the device. The device was fixed on a designed cantilever system which can apply axial strain to the ZnO NRAs with accurately controlled amplitudes.

Results and discussions

Figure 1b shows a cross-sectional SEM image of the ZnO NRAs, demonstrating a high density, well-aligned orientation, and clear surfaces. The average diameter of the nanorod (NR) is ~100 nm, and the average height is ~3.5 μm. Figure 1c and d

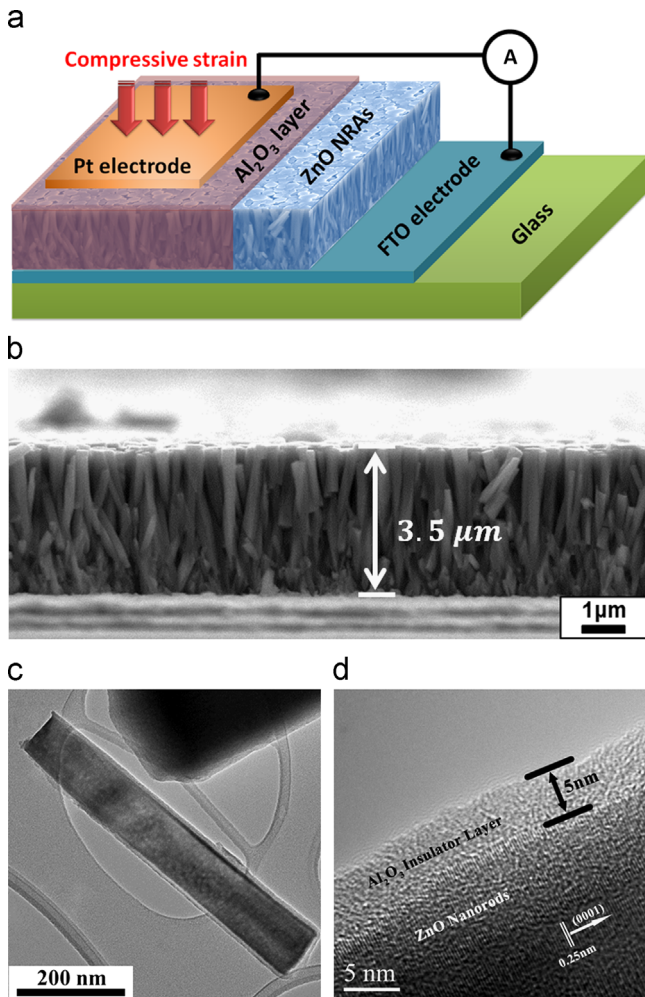


Figure 1 Structure and geometry of the NR-based photodetector. (a) A schematic diagram of the MIS structured photodetector. (b) The cross-sectional morphology of ZnO NRAs. The average height of NRAs is about 3.5 μm. (c) and (d) TEM and HRTEM images of an individual NR covered with a thin layer of Al₂O₃ respectively. The growth direction of ZnO NR and the thickness of the amorphous Al₂O₃ layer are marked in (d).

shows the TEM and the HRTEM images of an individual ZnO NR coated with a layer of Al₂O₃. A uniform Al₂O₃ layer with a thickness of 5 nm is observed completely covering the ZnO NR forming a core-shell nanostructure. The corresponding top view SEM images, XRD and EDX are shown in Figure S1 in Supporting information (SI). The total working area of the photodetector is determined by the size of Pt electrode, which is 0.0225 cm².

To illustrate the effect of the insulator layer at the interface, the performance of an MS structured junction is tested first, as shown in Figure 2a. The black and red lines are the dark and illuminated *I*-*V* curves, respectively. The reverse leakage current of the dark curve was measured ~6.43 mA at -1 V. This might be a result of lowered Schottky barrier height (SBH) at the ZnO-Pt interface, because the polar surfaces of ZnO can adsorb a certain amount of molecules forming an imaging-force to lower the barrier height [28,29]. Under illumination, the *I*-*V* curve changes to an approximately linear curve, suggesting that the Schottky barrier was screened by the charged surface states [30]. Figure 2b shows the *I*-*V* curve of a ZnO/Al₂O₃/Pt MIS contact, where the black and red lines are dark and illuminated curves, respectively. Under dark, the MIS junction exhibited an excellent rectifying behavior with a reverse leakage current of 4.68×10^{-4} mA at a bias of -1 V. The Al₂O₃ insulator layer effectively reduced the leakage current by 4 orders of magnitude compared to the ZnO/Pt contact. The insert of Figure 2b shows the curves of natural logarithm of current versus voltage, presenting a measurable photocurrent response at reverse bias. At bias of ±1 V, the rectification ratios of the MS and MIS junction can be calculated to be 4.04 and 794, respectively [31].

According to the Thermionic-Emission theory, the current transport process can be described as following [32]:

$$J_0 = A^* T^2 \exp\left(-\frac{q\phi_b}{kT}\right); \left(A^* = \frac{4\pi e m_n^* k^2}{h^3}, A_{ZnO}^* = 32 \text{ A cm}^{-2} \text{ K}^{-2}\right) \quad (1)$$

where J_0 is the current density at a fixed bias, A^* is the effective Richardson constant, T is the temperature, q is the unit electronic charge, ϕ_b is SBH, and k is the Boltzmann constant. Thus, the effective SBH (ϕ_b^*) can be simplified from Eq. (1) as following:

$$\phi_b^* = \phi_b - \phi_s = \frac{kT}{q} \left(\ln A^* T^2 - \ln \frac{I_0}{A} \right); \quad (2)$$

where ϕ_s is the SBH lowering induced by the surface state, and A is the working area which is 0.0225 cm² in this work. As a result, the calculated ϕ_b^* of the MIS junction is 0.739 eV which is much larger than that of the MS junction (0.47 eV). Under illumination, the barrier height of the MIS junction is slightly reduced by the photogenerated charges. For a SP photodetector, the photo response current is closely related to the amplitude of the built-in electric field and the amount of photogenerated charges. The thin insulator layer can prevent the surface adsorption and hence increase the effective barrier height. As a result, MIS junction is more suitable to be a SP photodetector.

Under the illumination of 100 mW/cm² and a bias of 0 V, the SP photodetector exhibited a measurable current variation and a distinct photoresponse (230.98%). Figure 2c and d shows the performance of the SP photodetector illuminated

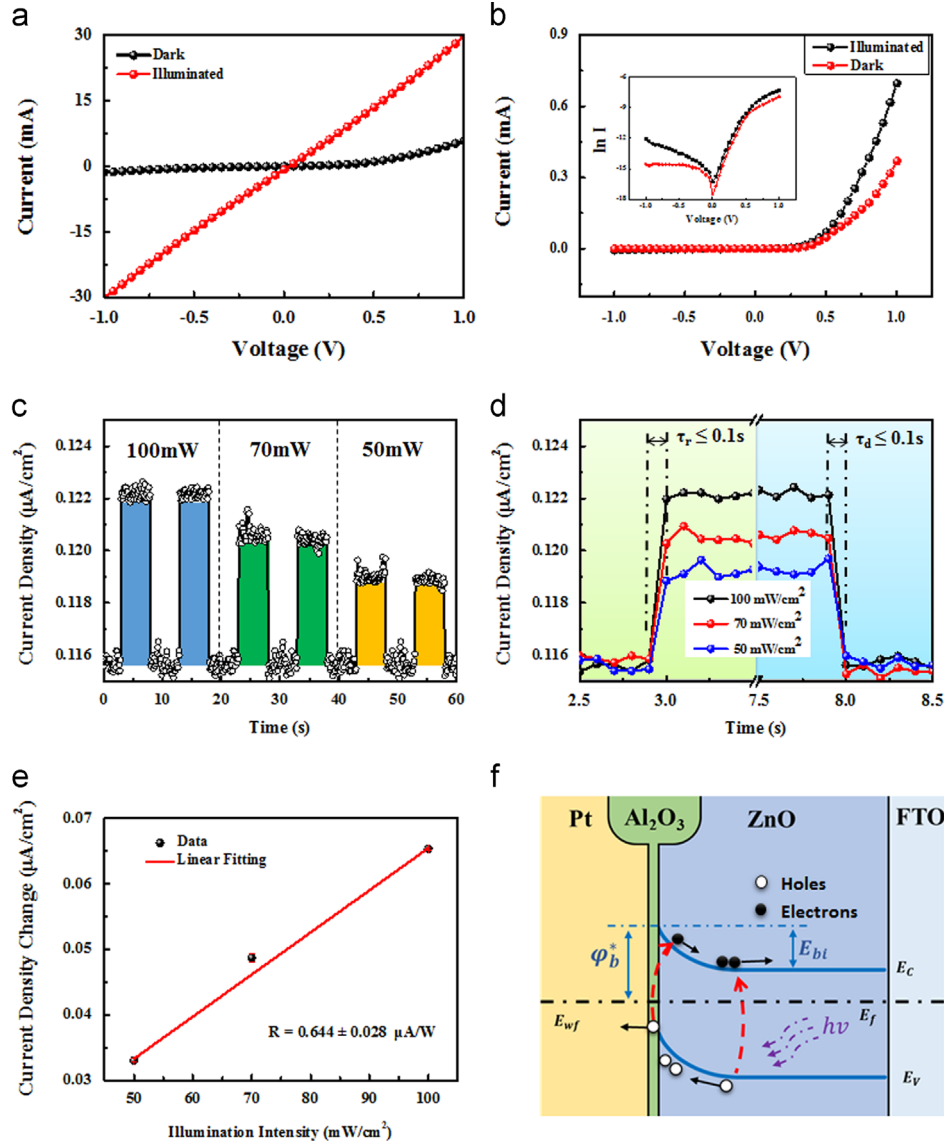


Figure 2 *I-V* characteristics of photodetectors. (a) *I-V* curves of a point-contact Schottky junction without insulator layer under dark and illumination. (b) *I-V* curves of a Schottky junction with insulator layer. Inset is the corresponding $\ln I$ -*V* curve. (c) and (d) The SP photocurrent responses of the MIS junction with different intensities of illumination at bias of 0 V. (e) The linear fitting curve of ΔJ_p versus light intensity, in which the slope of curve shows the responsivity (about $0.6 \mu\text{A}/\text{W cm}^2$). (f) The energy band diagram of the SP photodetector at zero bias.

under different light intensities. The SP photodetector demonstrated a constant photocurrent density (J_p) in response to the illuminations. The photocurrent density change (ΔJ_p) decreased from $0.0653 \mu\text{A}/\text{cm}^2$ under illumination of $100 \text{ mW}/\text{cm}^2$ to $0.0197 \mu\text{A}/\text{cm}^2$ at $50 \text{ mW}/\text{cm}^2$ [19]. Taking in the account of the time resolution of the testing system, the actual response time and decay time would be less than 0.1 s as measured in Figure 2d. In Figure 2e, a linear curve of ΔJ_p versus light intensity is fitted revealing that the responsivity (R) of the SP photodetector is $0.644 \pm 0.028 \mu\text{A}/\text{W}$. The normalized detectivity (D^*) is defined as [33]:

$$D^* = \frac{R}{\sqrt{2eJ_d}} \quad (3)$$

where R is the responsivity, J_d is the dark current density. Therefore, D^* was calculated to be $2.96 \times 10^6 \text{ cm Hz}^{0.5} \text{ W}^{-1}$.

A thermal equilibrium energy band schematic diagram at zero bias shown in Figure 2f illustrates the photo response process in an MIS SP photodetector. When the light illuminated at the heterostructure, EHPs are generated. The photogenerated holes drift toward the Pt electrode tunneling through the Al₂O₃ insulator layer, and the photogenerated electrons flow to the FTO electrode.

According to piezotronics theory, piezopolarization produced by the strained can make a constant influence toward the interface electronic properties including the depletion region and the barrier height [11,34]. The influence of piezopolarization on the barrier height of the SP photodetector is assessed under a series of compressive strains in dark. The strain is applied vertically onto the Pt electrode along the length direction of ZnO NRs by a cantilever system. The *I-V* curves in Figure 3a present that the current

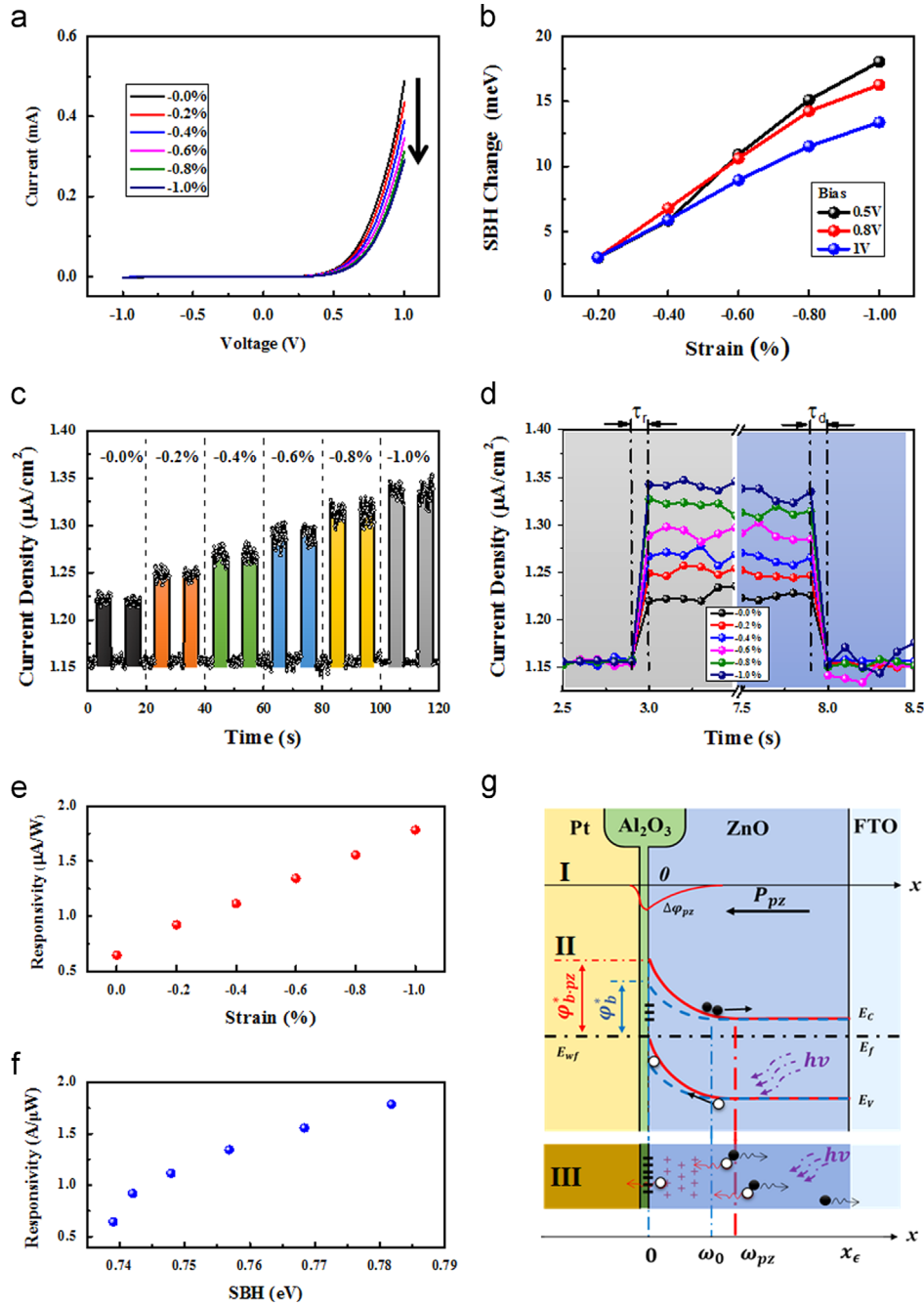


Figure 3 *I*-*V* characteristics of photodetectors under strain. (a) *I*-*V* curves under a series of compressive strains. (b) Calculated SBH change under compressive strains at different biases of 0.5 V, 0.8 V and 1 V. (c) The photoresponses at illumination of 100 mW/cm² under different compressive strains. (d) Detailed current density profiles of response process and recovery processes. (e) The relationship between responsivity and strain. (f) The relationship between responsivity and SBH. (g) The schematic diagram of the devices under compressive strain and illumination. I is the potential variation at the interface under a compressive strain. II is the band structure diagram. The blue dash line is the original energy band structure of the ZnO in a Schottky junction; the red solid line is the band structure under negative piezopolarization; and the black dash dot line is the Fermi level at thermal equilibrium. III illustrates a gradient piezo electric field formed in ZnO with a negative piezopolarization at the interface, which widens the depletion region from ω_0 to ω_{pz} .

reduced under compressive strain, suggesting that a piezo-induced negative polarization increased the SBH. Assuming A^* and T are constant under small strain, the SBH change ($\Delta\varphi$) can be derived from the Eq. (2) as following [35]:

$$\Delta\varphi = \varphi_{be} - \varphi_{b0} = -\frac{kT}{q} \ln(I_e/I_0) \quad (4)$$

where I_e and I_0 are the currents measured with and without being strained at a fixed forward bias, and φ_{be} and φ_{b0} are the corresponding SBH I_e and I_0 , respectively. The calculated results of $\Delta\varphi$ at biases of 0.5 V, 0.8 V and 1 V are plotted in Figure 3b. It demonstrates that the SBH increases linearly with the increase of compressive strain and is independent of external bias.

Figure 3c and d shows the photocurrent densities of the SP photodetector under compressive strains with an incident light intensity of 100 mW/cm^2 . For a Schottky junction under irradiation without an external power, the separation of photogenerated EHPs is caused by the built-in electric field (E_{bi}) which can be considered as a function of strain in the piezoelectric semiconductor. In this work, a constant photocurrent density ($J_{p-strain}$) was recorded under a fixed compressive strain. The photocurrent density changes ($\Delta J_{p-strain}$) increased monotonically with the compressive strain. As shown in Figure 4b, the measured response and recovery time under compressive strains are 0.1 s. The $J_{p-strain}$ of an MIS SP photodetector changed within 0.1 s in both response and recovery processes. The calculated responsivities under different strains are plotted in Figure 3e, showing the responsivity increased from 0.64 to $1.78 \mu\text{A/W}$. Based on Eq. (3), The detectivity of the SP photodetector are improve from 2.88×10^6 without strain to $7.99 \times 10^6 \text{ cmHz}^{0.5} \text{ W}^{-1}$ under compressive strain of -1.0% .

Figure 3g is a schematic diagram of the electronic band structure under compressive strain and illumination. When a compressive strain is applied vertically onto the Pt electrode along the length direction of a ZnO NR, a piezoelectric field is generated inside the ZnO NR with a negative polarization formed at the ZnO/Pt interface. This strain-induced polarization could modulate the depletion region in ZnO, the insulator layer, and the contact surface of Pt electrode. Because the mobility and the carrier concentration in Pt are much greater than ZnO and Al_2O_3 , the influence of piezopotential in Pt electrode occurs at the interface and decays rapidly. Due to the extremely small thickness of the Al_2O_3 layer, the potential reduction across Al_2O_3 is negligible [36]. Figure 3g I shows the potential variation at the interface in the presence of piezopolarization. In Figure 3g II, the blue dash line is the original energy band structure of ZnO, the red solid line is the band structure with negative piezopolarization, and the black dash dot line is the Fermi level at thermal equilibrium. Under compressive strain, the depletion region is widened from ω_0 to ω_{pz} by the negative piezopolarization. Such piezopolarization-enhanced built-in field and widened depletion region is favorable for photogenerated EHP separation, and thus rapid response and higher sensitivity are obtained.

According to Fowler theory, the photoresponse at zero bias is related to the intensity of incident light and the SBH [37]:

$$R^* \propto \frac{(h\nu - q\varphi_B)^2}{(q\varphi_B^* - h\nu)^{1/2}}, \text{ for } q\varphi_B < h\nu; \quad (5)$$

where R^* is the photoresponsivity, $h\nu$ is the intensity of incident light, φ_B is the theoretical SBH, φ_B is the effective SBH that can be enhanced by piezopotential. At a fixed incident light intensity ($h\nu = E_v$), and assuming the theoretical SBH to be the difference between the work function of Pt and the Fermi level of ZnO, R^* can be simply related to φ_B , which corresponds to the piezopotential induced by the strain. As shown in Figure 3f shown, the photoresponsivity increased monotonically with the barrier height.

To analyze the impact of piezotronic effect of ZnO, the relationship between resistance variation and applied voltage was measured by AC impedance characterization. Compared to a pn junction of which the impedance is dominated by the diffusion capacitance of the injected minority carriers, a Schottky junction can be equivalent to a series resistance (R_s) in connection to a pair of parallelly connected junction resistance (R_j) and junction capacitor (C_j), as shown in the inset of Figure 4a. At low frequencies, the capacitance in equivalent can be viewed as an open circuit. The variation of the total resistance ($R_s + R_j$) with applied bias across the junction under compressive strains is shown in Figure 4a. According to the Schottky junction theory, the total current, which consists of both thermionic emission and tunneling, can be modified as

$$I = I_s \left[\exp\left(\frac{qV_b - IR_s}{nkT}\right) - 1 \right] \quad (6)$$

where I_s is the saturation current obtained by extrapolating the current from log-linear plot to $V=0$, and n is the ideality factor. From Eq. (6), the differential resistance in the forward-bias region is dependent on the bias or current, given by

$$\frac{dV}{dI} = \frac{nkT + qIR_s}{qI} \quad (7)$$

This equation shows that the differential resistance of the diode at low bias is inversely proportional to the current ($=nkT/qI$). At high current when $IR_s \gg nkT/q$, the

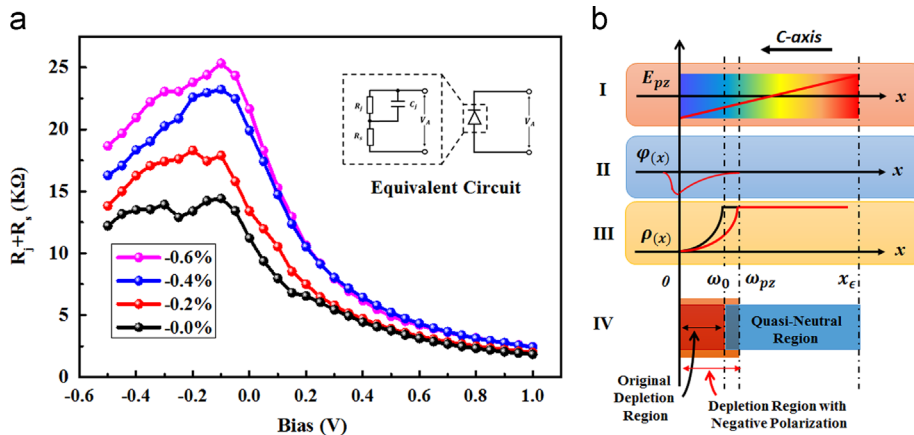


Figure 4 Resistance characterization. (a) Total resistance as a function of applied bias across the junction. Inset is the equivalent circuit of a Schottky junction. (b) A schematic diagram illustrating the relationship between the electric field (I), potential (II), the carrier concentration (III), and the depletion region (IV) induced by the piezopolarization under compressive strains.

differential resistance would saturate to the value of R_s [32]. Based on the junction theory, R_s can be described as following [38]

$$R_s = \frac{1}{A} \int_{w_f}^{w_0} \rho(x) dx + \frac{1}{A} \int_{w_0}^{x_c} \rho(x) dx + R_c; \quad (8)$$

where w_f and w_0 is the space charge boundaries at forward and zero bias respectively; x_c is the electrode contact boundary. The third term R_c is the resistance which is independent to the depletion region. The first term on the right hand represents the large fraction of the depletion layer at zero bias which will be collapsed under a higher forward bias, and the second term represents the resistance in quasi-neutral region. Therefore, the total resistance decreases rapidly with positive bias until the R_s dominates the effect of R_j . Typical values of R_s can be obtained from the right end of the curves in Figure 4a. The small changes in R_s under different compressive strains indicate that the device performances are barely affected by the variations of carrier concentration in ZnO. Meanwhile, the total resistances increased significantly at zero bias as the compressive strain increased. When the forward bias is close to zero, R_j , which is determined by the carrier concentration in the depletion region, plays a more important role in total resistance than R_s .

The schematic diagram in Figure 4b illustrates the relationship between the electric field (I), potential (II), the carrier concentration (III), and the depletion region (IV) induced by the piezopolarization under compressive strain. Under compressive strains, an electric field is induced by the piezopolarization generated inside ZnO. The negative polarization repels the electrons in ZnO away from the junction area yielding a reduced carrier concentration in the space charge region and an expanded depletion region. The built-in electric field varies with the redistribution of free charge carriers and thus modulates the SBH. In semiconductor materials, the resistivity can be described as following [32]

$$\rho(x) = \frac{1}{ne\mu_e}; \quad (9)$$

where n is the carrier concentration, μ_e is electron mobility, and e is unit electron charge. In ZnO NRs, μ_e and e are constants. Therefore, the resistivity is opposite proportion to the carrier concentration. Based on the data shown in Figure 4a, the smaller change of total resistance at forward bias and the dramatically increased junction resistance at zero bias suggest that the effect of piezopolarization is mostly implemented at the interface rather than inside the ZnO NRs. This result also evidences that the piezotronic effect is an effective approach for interface engineering in a MIS Schottky device.

Conclusions

In summary, a Pt/Al₂O₃/ZnO based MIS heterostructure SP photodetector was developed. The photodetector exhibited sensitive photoresponse to different light intensity without an external bias. The piezotronic modulation and introducing an insulating layer were applied to engineer the interface and enhance the photoresponse properties. By depositing a ~5 nm Al₂O₃ insulator layer at the interface, the effective SBH was increased to 0.739 eV. The responsivity and detectivity of the SP photodetector were found to be 0.644 μ A/W and 2.92×10^6 cm

Hz^{0.5} W⁻¹, respectively. The response and recovery time were less than 100 ms. When compressive strain was applied to the device, the piezopolarization modulated the built-in electric field at the interface and changed the SBH. As a result, the photoresponse properties of the SP photodetector were significantly improved. The responsivity and detectivity were raised to 1.78 μ A/W and 7.99×10^7 cm Hz^{0.5} W⁻¹, respectively under compressive strain of -1.0%. Based on the Schottky junction theory, it can be concluded that the piezotronic effect has the strongest influence on the interface and gradually decays towards the quasi-neutral region of the junction. This study further evidences that the piezotronic principle can be an effective approach for interface engineering to optimize the performance of Schottky junction-based electronic devices.

Acknowledgment

This work was supported by the National Major Research Program of China (2013CB932602), the Major Project of International Cooperation and Exchanges (2012DFA50990), the Program of Introducing Talents of Discipline to Universities, NSFC (51172022, 51232001, 51372020), the Fundamental Research Funds for the Central Universities, the Program for Changjiang Scholars and Innovative Research Team in University (FRF-SD-12-032 and FRF-AS-13-001). YY and XW thanks the support from National Science Foundation under Award CMMI-1148919. We thank Dr. Munho Kim from Prof. Zhanqiang Ma group in Department of Electrical and Computer Engineering, University of Wisconsin-Madison for his help for the Pt electrode fabrication.

Appendix A. Supporting information

The corresponding top view SEM images, XRD and EDX of the ZnO nanorod array covered with Al₂O₃, and the performance of the Pt electrode.

Supplementary data associated with this article can be found in the online version at <http://dx.doi.org/10.1016/j.nanoen.2014.07.019>.

References

- [1] B. O'regan, M. Grifitzi, Nature 353 (1991) 24.
- [2] Z.L. Wang, J. Song, Science 312 (2006) 242-246.
- [3] F.-R. Fan, Z.-Q. Tian, Z. Lin Wang, Nano Energy 1 (2012) 328-334.
- [4] Q. Liao, Z. Zhang, X. Zhang, M. Mohr, Y. Zhang, H.-J. Fecht, Nano Res. 7 (2014) 917.
- [5] X.M. Zhang, M.Y. Lu, Y. Zhang, L.J. Chen, Z.L. Wang, Adv. Mater. 21 (2009) 2767-2770.
- [6] X. Zhang, Y. Zhang, Q. Liao, Y. Song, S. Ma, Small 9 (2013) 4045-4050.
- [7] Y. Zhang, X. Yan, Y. Yang, Y. Huang, Q. Liao, J. Qi, Adv. Mater. 24 (2012) 4647-4655.
- [8] Y. Don Park, J.A. Lim, H.S. Lee, K. Cho, Mater. Today 10 (2007) 46-54.
- [9] Y. Zhang, Y. Liu, Z.L. Wang, Adv. Mater. 23 (2011) 3004-3013.
- [10] J. Shi, M.B. Starr, X. Wang, Adv. Mater. 24 (2012) 4683-4691.
- [11] X. Wang, Am. Ceram. Soc. Bull. 92 (2013) 18-23.
- [12] J. Shi, P. Zhao, X. Wang, Adv. Mater. 25 (2013) 916-921.

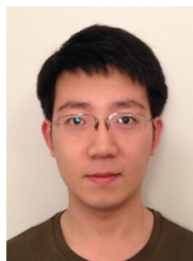
- [13] C. Pan, L. Dong, G. Zhu, S. Niu, R. Yu, Q. Yang, Y. Liu, Z.L. Wang, *Nat. Photon.* 7 (2013) 752-758.
- [14] R. Yu, C. Pan, Y. Hu, L. Li, H. Liu, W. Liu, S. Chua, D. Chi, Z. L. Wang, *Nano Res.* 6 (2013) 758.
- [15] Q. Yang, X. Guo, W. Wang, Y. Zhang, S. Xu, D.H. Lien, Z. L. Wang, *ACS Nano* 4 (2010) 6285.
- [16] S. Xu, Y. Qin, C. Xu, Y. Wei, R. Yang, Z.L. Wang, *Nat. Nanotechnol.* 5 (2010) 366-373.
- [17] Z.L. Wang, *Adv. Mater.* 24 (2012) 280-285.
- [18] Z. Zhang, Q. Liao, X. Yan, Z.L. Wang, W. Wang, X. Sun, P. Lin, Y. Huang, Y. Zhang, *Nano Res.* 7 (2013) 190-198.
- [19] Y. Yang, L. Lin, Y. Zhang, Q. Jing, T.C. Hou, Z.L. Wang, *ACS nano* 6 (2012) 10378-10383.
- [20] Y. Hu, Y. Zhang, C. Xu, L. Lin, R.L. Snyder, Z.L. Wang, *Nano Lett.* 11 (2011) 2572-2577.
- [21] Y.Q. Bie, Z.M. Liao, H.Z. Zhang, G.R. Li, Y. Ye, Y.B. Zhou, J. Xu, Z.X. Qin, L. Dai, D.P. Yu, *Adv. Mater.* 23 (2011) 649-653.
- [22] S.M. Hatch, J. Briscoe, S. Dunn, *Adv. Mater.* 25 (2013) 867-871.
- [23] Y. Yang, W. Guo, J. Qi, J. Zhao, Y. Zhang, *Appl. Phys. Lett.* 97 (2010) 223113.
- [24] W. Jin, Y. Ye, L. Gan, B. Yu, P. Wu, Y. Dai, H. Meng, X. Guo, L. Dai, *J. Mater. Chem.* 22 (2012) 2863-2867.
- [25] L. Peng, L.F. Hu, X.S. Fang, *Adv. Funct. Mater.* 24 (2014) 2591.
- [26] C.-H. Lin, C.W. Liu, *Sensors* 10 (2010) 8797-8826.
- [27] M. Bayindir, F. Sorin, A.F. Abouraddy, J. Viens, S.D. Hart, J.D. Joannopoulos, Y. Fink, *Nature* 431 (2004) 826-829.
- [28] C. Woll, *Prog. Surf. Sci.* 82 (2007) 55-120.
- [29] A. Cowley, S. Sze, *J. Appl. Phys.* 36 (2004) 3212-3220.
- [30] Y. Jin, J. Wang, B. Sun, J.C. Blakesley, N.C. Greenham, *Nano Lett.* 8 (2008) 1649-1653.
- [31] Q. Pei, G. Yu, C. Zhang, Y. Yang, A.J. Heeger, *Science* 269 (1995) 1086-1088.
- [32] S. Sze, K.K. Ng, *Phys. Semicond. Devices*, John Wiley & Sons, Inc., Hoboken, New Jersey, 2006.
- [33] C.-H. Lin, C.-Y. Yu, C.-Y. Peng, W. Ho, C. Liu, *J. Appl. Phys.* 101 (2007) 033117-033117-033114.
- [34] Z.L. Wang, W. Wu, *Natl. Sci. Rev.* 1 (2013) 62-90.
- [35] J. Zhou, Y. Gu, P. Fei, W. Mai, Y. Gao, R. Yang, G. Bao, Z.L. Wang, *Nano Lett.* 8 (2008) 3035-3040.
- [36] R. Hinchet, S. Lee, G. Ardila, L. Montès, M. Mouis, Z.L. Wang, *Adv. Funct. Mater.* 24 (2014) 971-977.
- [37] R.H. Fowler, *Phys. Rev.* 38 (1931) 45.
- [38] H.A. Watson, M.R. Barber, *Microwave Semiconductor Devices and Their Circuit Applications*, McGraw-Hill, New York, 1969.



Zheng Zhang is currently a Ph.D. candidate at the school of Material Science and Engineering, University of Science and Technology Beijing, Beijing, China. His research interests focus on ZnO based electromechanical nanodevice, self-powered nanodevices, and piezotronics.



Qingliang Liao received his Ph.D. degree from University of Science and Technology Beijing (USTB) in 2009. Now he is an associate professor at School of Materials Science and Engineering in USTB. His scientific interests focus on synthesis and characterization of one-dimensional nanomaterials, design and application of functional nanodevices.



Yanhao Yu is currently a Ph.D. candidate of Materials Engineering at University of Wisconsin-Madison under the supervision of Prof. Xudong Wang. He received his B.S. degree in Chemical Engineering at Dalian University of Technology, China in 2011. His current research focuses on the growth and integration of functional oxide nanomaterials for the applications of photovoltaics and photoelectrochemical water splitting.



Xudong Wang is an assistant professor in the department of Materials Science and Engineering at University of Wisconsin-Madison. His research interests include studying the growth and assembly of oxide nanowire arrays, understanding the coupling effect of semiconductor properties and piezoelectric charge displacement, and developing nanogenerator that uses piezoelectric nanomaterials to convert low level mechanical energy into electricity. He is the recipient of NSF CAREER Award, DARPA Young Faculty Award, 3M Non-Tenured Faculty Award, Ross Coffin Purdy Award, Young Innovators Under 35 Award, and KAUST research fellow. He has published 62 papers in peer reviewed scientific journals, contributed 7 book chapters in his research field, and holds 5 patents/provisional patents on oxide nanostructures and nanomaterial-enhanced energy harvesting. His publications have been cited over 6000 times by peers and his current hindex is 34.



Yue Zhang is a professor of Material Physics and vice-president of University of Science and Technology Beijing, China. He has been awarded the financial support for outstanding young scientist foundation of China and selected as the chief scientist of Major National Scientific Research Projects. His research focuses on functional nanomaterials and nano-devices, new energy materials, and nanoscale failure and service behavior. He has published more than 270 papers in peer reviewed scientific journals and 8 monograph, and held 25 patents in his research area. His publication has been cited more than 2000 times by peers.